Journal of Micromechanics and Microengineering

You may also like

- Active control of the nonlinear static and dynamic responses for piezoelectric viscoelastic microplates
  Yiming Fu and Jin Zhang
- Pull-in dynamics of overdamped microbeams
  Michael Gomez, Dominic Vella and Derek E Moulton
- The pull-in behavior of electrostatically actuated bistable microstructures
  Slava Krylov, Bojan R Ilic, David Schreiber et al.

Control of pull-in dynamics in a nonlinear thermoelastic electrically actuated microbeam

To cite this article: Stefano Lenci and Giuseppe Rega 2006 *J. Micromech. Microeng.* **16** 390

View the article online for updates and enhancements.

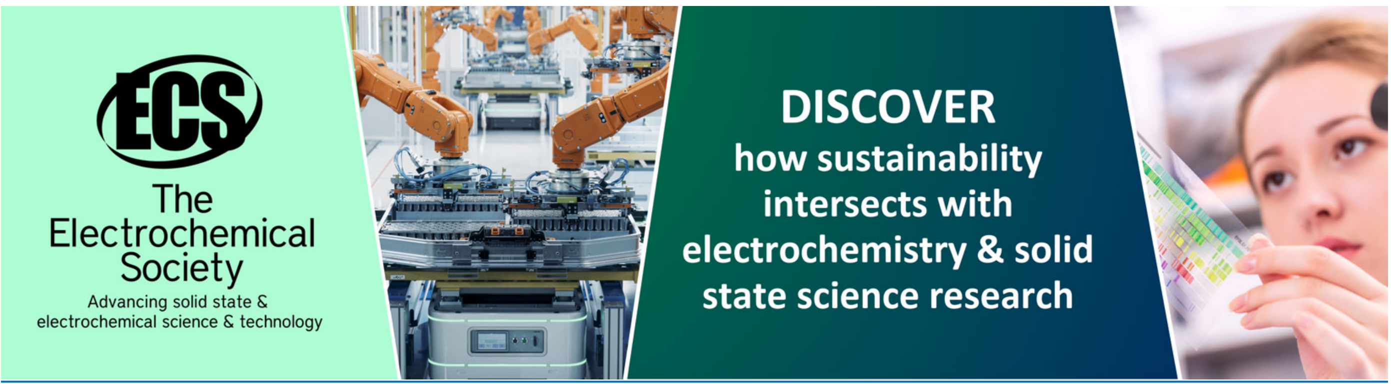

This content was downloaded from IP address 18.117.216.229 on 04/05/2024 at 22:02

J. Micromech. Microeng. **16** (2006) 390–401 doi:10.1088/0960-1317/16/2/025

Control of pull-in dynamics in a nonlinear thermoelastic electrically actuated microbeam

Stefano Lenci[1] **and Giuseppe Rega**[2]

[1] Dipartimento di Architettura, Costruzioni e Strutture, Università Politecnica delle Marche via Brecce Bianche, 60131, Ancona, Italy

[2] Dipartimento di Ingegneria Strutturale e Geotecnica, Università di Roma "La Sapienza" via A Gramsci 53, 00197, Roma, Italy,

E-mail: Lenci@univpm.it and Giuseppe.Rega@uniroma1.it

Received 22 July 2005, in final form 7 December 2005
Published 19 January 2006
Online at stacks.iop.org/JMM/16/390

Abstract
This work deals with the problem of controlling the nonlinear dynamics, in general, and the dynamic pull-in, in particular, of an electrically actuated microbeam. A single-well softening model recently proposed by Gottlieb and Champneys [1] is considered, and a control method previously proposed by the authors is applied. Homoclinic bifurcation, which triggers the safe basin erosion eventually leading to pull-in, is considered as the undesired event, and it is shown how appropriate controlling superharmonics added to a reference harmonic excitation succeed in shifting it towards higher excitation amplitudes. An optimization problem is formulated, and the optimal excitation shape is obtained. Extensive numerical simulations aimed at checking the effectiveness of the control method in shifting the erosion of the safe basin are reported. They highlight good performances of the control method beyond theoretical expectations.

(Some figures in this article are in colour only in the electronic version)

1. Introduction

Microelectromechanical systems, or MEMS, are an emerging area with applications to a variety of engineering fields such as aerospace, mechanics, electricity, communications, bioengineering and sport devices. MEMS are a new technology which exploits existing microelectronic infrastructures to create complex machines with micrometre feature sizes. These machines have many functions, including sensing and actuation. MEMS are often constituted by standard structural elements such as (micro)beams and (micro)plates, and classical theories usually do apply.

Two main aspects seem to have mostly been addressed in the recent MEMS literature. The first is the mechanical modelling [2], required to fill the lack of knowledge of these relatively new systems. Examples of phenomena which have been specifically considered are various kinds of nonlinearities [3], such as nonlinear stiffness [4], thermoelastic damping [5], micro-impacts [6], complex (Cosserat) models for microbeam [7, 8], atomic forces [9], and so on.

The second is the dynamic behaviour, which is a key point from the application viewpoint. Several specific issues have been dealt with, ranging from dynamical reduced-order models [10, 11–14], to nonlinear dynamics and chaos [15– 17], which are sometimes investigated by the Melnikov method [18, 19] and experimentally [20]. Complex dynamics is seen to be a common outcome for these strongly nonlinear systems, although much remains to be done in this area.

Among various nonlinear phenomena, the pull-in, i.e., the collapse of the microbeam on the charged substrate, is the most important one, and it has been investigated with both statical (i.e., dc) [10] and dynamical (i.e., ac) [21, 22] applied voltages. It has been shown that dynamic excitation usually strongly reduces the static pull-in threshold. While in micro-switches this is desirable because it improves the performance of the system, in common MEMS devices, such as micro-resonators, micro-sensors, etc, this is unwanted because it leads to failure of the structures, and must be avoided or properly detected.

The dynamic pull-in phenomenon entails overcoming the energy level of the saddle position(s) in between the rest state and the substrate(s), for which the electric and elastic force balance in unstable way. It is similar to the escape from the potential well observed in classical mechanical oscillators [23, 24], and is related to the global (homo/heteroclinic) bifurcation of the hilltop saddle(s) through a known mechanism [23–25]. A global bifurcation is the event through which the stable manifold of a certain saddle becomes tangent to the unstable manifold of the same (homoclinic) or of another (heteroclinic) saddle. This occurs at a certain critical value $p_{\rm cr}$ of a varying governing parameter p. For $p < p_{\rm cr}$ (respectively $p > p_{\rm cr}$) the manifolds are detached, while for $p > p_{\rm cr}$ (respectively $p < p_{\rm cr}$) the manifolds intersect transversally (see [26] for further details).

Before the global bifurcation, the in-well dynamics is safe; after, the homo/heteroclinic intersections allow (and somehow promote) penetration of the fractal tongues of the basin(s) of attraction of the pull-in attractor(s) into the potential well. These tongues erode the safe basin, so that the extent (in phase space) of initial conditions leading to pull-in grows, and system safety and reliability decrease. When the excitation amplitude further grows, the erosion proceeds up to complete destruction of the safe basin; this represents the ultimate state, above which *all* initial conditions lead to pull-in, and the MEMS fails.

Previous considerations show that below the global bifurcation, pull-in does not occur, while above it becomes impending, although reduced safe dynamics can still occur. Thus, shifting the global bifurcation threshold permits us to enlarge the region where pull-in is prevented, and represents a very desiderable event. This is the main practical objective of this work, which is also aimed at addressing the issue of controlling MEMS dynamics; this still deserves much work because it has only been investigated preliminarily [16, 19], up to the authors' knowledge. Furthermore, the application of control of chaos theories [27] seems to be another element of novelty of this work (see also [28]).

A method for controlling nonlinear dynamics and chaos previously developed by the authors [23, 29] and based on shifting the bifurcation threshold by optimally modifying the excitation *shape*, i.e., on adding controlling superharmonics to a reference harmonic excitation, is employed. The method is not aimed at controlling a specific orbit of the system, as in classical control techniques, but rather, as a consequence of the shift of the homoclinic bifurcation, at obtaining an overall control of the dynamics, in general, and at enlarging in parameters space the region certainly safe from pull-in, in particular.

To analytically detect the homoclinic bifurcation, which is the keypoint for application of control, the classical Melnikov method is used [1, 18, 19]. This permits feasible computations and the use of generic results concerning control obtained elsewhere [23, 29].

Although the fully nonlinear dynamics is described by partial differential equations (PDEs), to study the main aspects of the nonlinear dynamics of MEMS, and to apply the control method, a reduced-order model, described by ordinary differential equations (ODEs), can be satisfactory, provided the initial PDEs are sufficiently accurate. This permits feasible analyses and computations, without losing the main dynamical aspects. Indeed, a single degree of freedom model is sufficient for the purposes of this work. In this respect, we refer to [1], where a model of a thermoelastic microbeam for a MEM sensor subjected to electrodynamic actuation is proposed.

Gottlieb and Champneys [1] obtained sophisticated two-field PDEs taking into account nonlinear membrane stiffness and the thermoelastic field, and focused on two-field single mode dynamics. The three resulting ODEs are Hamiltonian plus perturbations due to electrodynamic force, viscoelastic damping and thermoelastic dissipation. Because of the electrical force, the Hamiltonian exhibits the $(1 - x)^{-1}$ singularity typical of MEMS, which entails a single-well potential surrounded by the homoclinic loop of a hilltop saddle. The Melnikov method for determining the homoclinic bifurcation in the presence of perturbations was applied, and the resulting threshold was used to estimate the pull-in threshold from below.

The main modification of the present work to the model of [1] consists in applying a periodic alternate voltage between the beam and the substrate, $\mathsf{V}(\tau) = \mathsf{V}_1 \sin(\omega\tau + \psi_1) + \sum_{j=2}^{N} \mathsf{V}_j \sin(j\omega\tau + \psi_j)$. This is at the base of the control method, which uses the superharmonics V_j added to the basic harmonic voltage V_1 to control the dynamics. Indeed, it is the control itself to suggest the optimal choice of these controlling terms.

It is worth noting that, although we explicitly refer to the model of Gottlieb and Champneys [1], similar, or identical, equations have been independently obtained in the literature to describe the single mode dynamics of various MEMS devices [10, 21]. All of them share the property of having the charged substrate only on one side of the microbeam, so that pull-in can occur only in one direction. MEMS with substrates on both sides, and thus with two pull-in directions, have also been studied [12], but the underlying ODEs are different from those used in this work, so that the results of this work do not extend immediately to those cases.

The paper is organized as follows. First, the exact reduced-order model and its unperturbed dynamics are addressed (section 2), along with the Melnikov analysis which permits theoretical detection of the homoclinic bifurcation (section 3). In spite of the fact that the unperturbed homoclinic loop can be written in implicit form, the Melnikov function cannot be computed in closed form, and is determined by numerically computing the appropriate integrals.

Then, the control method is applied (section 4), by stating the optimization problem for the best excitation shape. It is the same problem encountered in the analysis of different mechanical systems, which (i) further confirms the generality of the control method discussed in [29], and (ii) permits to take advantage from previous solutions, which are herein extended to the present case. Among various possible solutions [29], those with a finite number of added superharmonics are considered because they are most interesting for applications. It is shown that with a single controlling superharmonic the homoclinic bifurcation threshold increases by a frequency-independent factor of 1.4142 with respect to the reference case of harmonic excitation, while the theoretical upper bound for this ratio, corresponding to infinite superharmonics, is 2.

Finally, the results of numerical simulations aimed at checking the practical performances of control, and

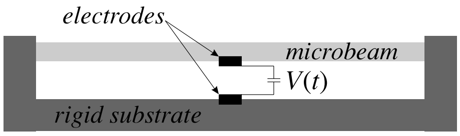

Figure 1. A schematic picture of the electrically actuated microbeam.

in particular how much its effectiveness extends beyond theoretical predictions, are reported in section 5, and the paper ends with some conclusions (section 6).

2. Mechanical model, governing equations and unperturbed dynamics

We consider the nonlinear dynamics of a thermoelastic rectangular microbeam subjected to an axial load (possibly modelling residual stresses due to manufacturing processes) and to a concentrated electrodynamic transverse force applied at mid-span (the actuation). The beam is fixed at both ends and is in an ultra-high vacuum environment (figure 1); the geometric nonlinearity due to the membrane stiffness is taken into account.

The two nonlinear partial differential equations governing the problem and permitting us to determine the unknown fields of transverse displacement and temperature were determined by Gottlieb and Champneys [1], who are referred to for the details of the analysis. The main physical change made in this work with respect to Gottlieb and Champneys' model stands in considering a non-harmonic, though still periodic, oscillating voltage $\mathsf{V}(\tau) = \mathsf{V}_1 \sin(\omega\tau + \psi_1) + \sum_{j=2}^{N} \mathsf{V}_j \sin(j\omega\tau + \psi_j)$, while they use only harmonic ac, $\mathsf{V}(\tau) = \mathsf{V}_1 \sin(\omega\tau)$. The more general excitation will appear to be useful in the control procedure. In any case, it adds to the electrostatic (dc) voltage V_0.

A two-field ($x(t)$, transverse displacement and $z(t)$, temperature) reduced-order model was also obtained in [1] by the Galerkin method. The transverse displacement spatial mode shape is the first resonant bending mode, while the temperature spatial mode shape is obtained by solving the homogeneous governing equations with no heat flow across the boundaries of the beam. The *dimensionless* equations of motion for the modal amplitudes read [1]

$$\begin{aligned} \dot{x} &= y, \\ \dot{y} &= \gamma \frac{\left[1 + \sum_{j=1}^{N} \eta_j \sin(j\Omega t + \Psi_j)\right]^2}{(1-x)^2} \\ &\quad - \alpha x - \beta x^3 - \mu_1 y - \mu_2 z, \\ \dot{z} &= -\nu z + \sigma y, \end{aligned} \tag{1}$$

and represent the starting point for the present analysis. Note that $y(t)$ is the velocity in the transversal direction. The dimensionless parameters in (1) have the following meaning:

- α is the linear mechanical stiffness, which accounts for the bending stiffness plus the effect of the axial force. It is positive below the critical threshold for buckling, and negative above it.
- $\beta > 0$ is the nonlinear mechanical stiffness parameter due to the membrane effect, which is approximated to the third order.

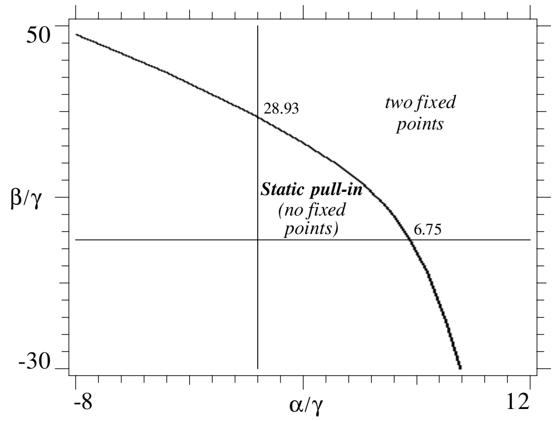

Figure 2. Regions of different behaviour.

- $\mu_1 > 0$ is the viscoelastic structural damping.
- $\mu_2 > 0$ and σ are the thermoelastic damping measuring the energy dissipation due to thermal effects, and the coupling between thermal and mechanical behaviour of the beam, respectively. They depend on the relaxation strength ΔE of the elastic Young's modulus, on the coefficient of thermal expansion, and on the equilibrium temperature.
- $\nu > 0$ is the thermal diffusivity.
- $\gamma > 0$ is the magnitude of the electrostatic force, which is proportional to the square of the constant (dc) part V_0 of the input voltage.
- Ω is the frequency of the periodic electrodynamic force, i.e., the frequency of the alternate current.
- Ψ_j and $\eta_j = \mathsf{V}_j/\mathsf{V}_0 > 0$ are the phases and the relative amplitudes of the jth harmonic of the electrodynamic force, i.e., of the oscillating (ac) voltage. In [1] only the case $N = 1$ is considered.

The gap between the beam and the source of the electric force (the substrate) is normalized to 1.

The third-order dynamical system (1) is constituted by a Hamiltonian part (α, β, γ), plus visco- and thermoelastic damping ($\mu_1, \mu_2, \sigma, \nu$) and periodic electrodynamic excitation (Ω, η_j, Ψ_j). The associated Hamiltonian $H(x, y)$ and potential $V(x)$ are

$$H(x, y) = \frac{y^2}{2} + V(x), \qquad V(x) = \alpha\frac{x^2}{2} + \beta\frac{x^4}{4} - \frac{\gamma}{1-x}. \tag{2}$$

Qualitatively, there are only two different scenarios for (2). When the electric force is high enough there are no equilibrium points and the beam collapses onto the substrate, i.e., we have static pull-in. When γ is small, on the other hand, the electric and mechanical forces balance with each other and two equilibrium positions appear, one elliptic centre $x_c > 0$ and one hyperbolic saddle $x_s > x_c > 0$ (figure 3(*b*)). In the parameters space the boundary between these two regions is the curve of figure 2, which corresponds to a SN bifurcation.

The dynamics are non-trivial only in the case of two fixed points. An archetypal potential and the corresponding phase space are depicted in figure 3 for $\alpha = \beta = 1$ and $\gamma = 0.14$. These values correspond to a microbeam–substrate gap equal to the height of the beam [1], and will be used in the forthcoming numerical simulations.

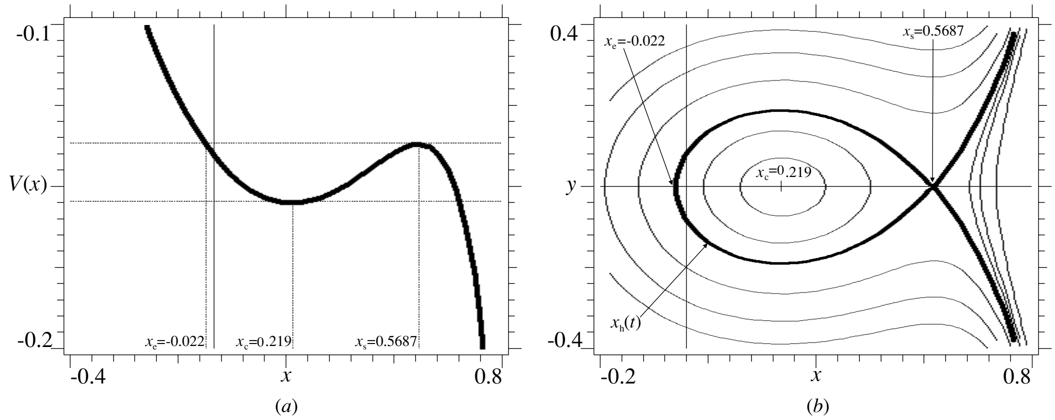

Figure 3. (*a*) The potential $V(x)$ and (*b*) the unperturbed phase space for $\alpha = \beta = 1$ and $\gamma = 0.14$.

There is a unique potential well with a right (towards the substrate $x = 1$) pull-in direction (figure 3(*a*)), showing that the system is of softening type. There are in-well oscillations around the centre $x_c = 0.219\,03$ and out-of-well orbits which are separated by the homoclinic loop $x_h(t)$ of the hilltop saddle $x_s = 0.568\,71$ (figure 3(*b*)). The homoclinic orbit, which is an even function of the time t, is implicitly defined by

$$\begin{aligned} y_h &= \frac{\mathrm{d}x_h}{\mathrm{d}t} = \pm\sqrt{2[V(x_s) - V(x)]} \quad \rightarrow \\ t &= t(x) \\ &= \pm \int_{x_e}^{x} \frac{\mathrm{d}r}{\sqrt{2[V(x_s) - V(r)]}}, \end{aligned} \tag{3}$$

where $x_e = x_h(0)$ is the extreme position of the homoclinic orbit (figure 3) and the unique solution (apart from x_s) of $V(x) = V(x_s)$. Unfortunately, the integral in (3) cannot be expressed in closed form, but it can be computed numerically in spite of being singular at both ends $x = x_e(t = 0)$ and $x = x_s(t = \pm\infty)$.

Hereinafter, it is assumed that the electrodynamic force is a small perturbation of the electrostatic one ($\eta_j = \varepsilon\hat{\eta}_j$, ε is a smallness parameter), and that the viscous structural damping is small as well ($\mu_1 = \varepsilon^k\hat{\mu}_1$). The relative sizes of these quantities, given by k, are very important, especially for practical applications, and various cases can be considered. In this paper, only the most simple case of comparable smallnesses is considered, i.e., we assume $k = 1$. The other cases are worth but they are out of the scope of the present work.

It has been shown in [1] that $\mu_2\sigma \approx \Delta E$ [1]. Consequently, as the relaxation strength ΔE is typically very small [5], it makes sense to consider two limit configurations [1]. In the first, it is assumed that μ_2 is not small while $\sigma = \varepsilon\hat{\sigma}$ and $\nu = \varepsilon\hat{\nu}$ are small quantities. In this case, the system (1) can be rewritten in the form

$$\begin{aligned} \dot{x} &= y, \\ \dot{y} &= \left\{\frac{\gamma}{(1-x)^2} - \alpha x - \beta x^3 - \mu_2 z\right\} \\ &\quad + \varepsilon\left\{-\mu_1 y + \frac{2\gamma}{(1-x)^2}\sum_{j=1}^{N}\eta_j \sin(j\Omega t + \Psi_j)\right\}, \\ \dot{z} &= \varepsilon\{-\nu z + \sigma y\}, \end{aligned} \tag{4}$$

where the hats are omitted to simplify the notation and the ε^2 terms are neglected.

In the second, on the other hand, it is assumed that $\mu_2 = \varepsilon\hat{\mu}_2$ is small while σ and ν are large. In this case, the general solution $z(t) = z_0\,\mathrm{e}^{-\nu t} + \sigma\int_0^t y(\tau)\,\mathrm{e}^{\nu(\tau-t)}\,\mathrm{d}\tau$ of the third equation in (1) can be rewritten in the form

$$z(t) = z_0\,\mathrm{e}^{-\nu t} + \frac{\sigma}{\nu}\int_{-\nu t}^{0} y\left(t + \frac{s}{\nu}\right)\mathrm{e}^{s}\,\mathrm{d}s, \tag{5}$$

where the change of variable $s = \nu(\tau - t)$ has been used in the integral. When ν is large, we have that $\mathrm{e}^{-\nu t} \approx 0$, $y(t + s/\nu) \approx y(t)$, $\int_{-\nu t}^{0}\mathrm{e}^{s}\,\mathrm{d}s \approx 1$, so that (5) simplifies to $z(t) = (\sigma/\nu)y(t)$ (note that it does not vanish because σ and ν have the same order of magnitude in this case), namely, the temperature can be condensed. This yields the following second-order system,

$$\begin{aligned} \dot{x} &= y, \\ \dot{y} &= -V'(x) + \varepsilon f(x, y, t) = \left\{\frac{\gamma}{(1-x)^2} - \alpha x - \beta x^3\right\} \\ &\quad + \varepsilon\left\{-\tilde{\mu} y + \frac{\tilde{\eta}}{(1-x)^2}\sum_{j=1}^{N}\left(\frac{\eta_j}{\eta_1}\right)\sin(j\Omega t + \Psi_j)\right\}, \end{aligned} \tag{6}$$

where again the hats are omitted and the ε^2 terms are neglected. In equation (6) $\tilde{\mu} = \mu_1 + (\sigma/\nu)\mu_2 > 0$ is the overall damping, $\tilde{\eta} = 2\gamma\eta_1 > 0$ is the overall excitation amplitude, while the parameters η_j/η_1 (together with the phases Ψ_j) simply govern the shape of the excitation, or, in other words, they measure the superharmonic relative corrections to the basic harmonic excitation.

We focus on the one-field system (6). The two-field system (4) can be dealt with through a modified Melnikov analysis [26].

3. Melnikov analysis

Figure 3(*b*) clearly shows how in the Hamiltonian case the homoclinic loop separates the safe in-well oscillations from dangerous pull-in motions, and thus represents a barrier for confined motions. When perturbations are added ($\varepsilon > 0$), stable and unstable manifolds of x_s split, and they may or may not intersect depending on the relative magnitude of damping $\tilde{\mu}$ and excitation $\tilde{\eta}$. It is known [23, 24] that when they intersect the barrier is lost, and the tongues of the basin of the substrate attractor penetrate the potential well (see forthcoming figure 9), erode the safe basin until, for a sufficiently high excitation amplitude, it is totally destroyed. This corresponds to the structure being pulled into the substrate for all initial conditions, i.e., to definitive dynamic pull-in.

The complex mechanism eventually leading to failure is triggered by the homoclinic bifurcation of the hilltop saddle, which occurs when the stable and unstable manifolds become tangent. This important critical threshold can be detected by the Melnikov method [26].

The Melnikov function measuring the first-order (in ε) distance between perturbed stable and unstable manifolds is given by

$$\begin{aligned}\mathsf{M}(t_0) &= \int_{-\infty}^{\infty} y_h(t) f[x_h(t), y_h(t), t+t_0]\,\mathrm{d}t \\ &= -\tilde{\mu}\int_{-\infty}^{\infty} y_h^2(t)\,\mathrm{d}t + \tilde{\eta}\sum_{j=1}^{N}\left(\frac{\eta_j}{\eta_1}\right) \\ &\quad\times \int_{-\infty}^{\infty}\frac{y_h(t)}{[1-x_h(t)]^2}\sin[j\Omega(t+t_0)+\Psi_j]\,\mathrm{d}t \\ &= -2\tilde{\mu}I_1 + 2\tilde{\eta}\sum_{j=1}^{N}\left(\frac{\eta_j}{\eta_1}\right)\cos(j\Omega t_0+\Psi_j)I_2(j\Omega) \\ &= 2\tilde{\mu}I_1\left\{-1+\tilde{\eta}\frac{I_2(\Omega)}{\tilde{\mu}I_1}h(\Omega t_0)\right\},\end{aligned} \qquad (7)$$

where the following relations and definitions have been used:

$$\begin{aligned}&\int_{-\infty}^{\infty} y_h^2(t)\,\mathrm{d}t = 2\int_0^{\infty} y_h^2(t)\,\mathrm{d}t = 2\int_0^{\infty} y_h(t)\frac{\mathrm{d}x_h}{\mathrm{d}t}(t)\,\mathrm{d}t \\ &= 2\int_{x_e}^{x_s} y_h(x)\,\mathrm{d}x = 2I_1 > 0, \\ &\int_{-\infty}^{\infty}\frac{y_h(t)}{[1-x_h(t)]^2}\sin[\omega(t+t_0)+\Psi_j]\,\mathrm{d}t \\ &= \cos(\omega t_0+\Psi_j)\int_{-\infty}^{\infty}\frac{y_h(t)}{[1-x_h(t)]^2}\sin(\omega t)\,\mathrm{d}t \\ &\quad+\sin(\omega t_0+\Psi_j)\int_{-\infty}^{\infty}\frac{y_h(t)}{[1-x_h(t)]^2}\cos(\omega t)\,\mathrm{d}t \\ &= 2\cos(\omega t_0+\Psi_j)\int_0^{\infty}\frac{y_h(t)}{[1-x_h(t)]^2}\sin(\omega t)\,\mathrm{d}t \\ &= 2\cos(\omega t_0+\Psi_j)\int_{x_e}^{x_s}\frac{1}{(1-x)^2} \\ &\quad\times\sin\left(\omega\int_{x_e}^{x}\frac{\mathrm{d}r}{\sqrt{2[V(x_s)-V(r)]}}\right)\mathrm{d}x \\ &= 2\cos(\omega t_0+\Psi_j)I_2(\omega), \qquad \omega = j\Omega,\end{aligned}$$

$$h(m) = \sum_{j=1}^{N} h_j\cos(jm+\Psi_j), \qquad h_j = \frac{\eta_j}{\eta_1}\frac{I_2(j\Omega)}{I_2(\Omega)}. \qquad (8)$$

Remark 1. Note that $h_1 = 1$, $h(m)$ is 2π—periodic and has zero mean value, and that $2I_1$ is the area inside the homoclinic loop in figure 3(*b*). Note also that the phase Ψ_1 is unessential and can be chosen freely.

The function $I_2(\Omega)$, which is central in the previous formulae, is depicted in figure 4 for various values of the linear stiffness α. For next purposes, the most important feature is that it is an oscillating function exponentially converging to zero for $\Omega \to \infty$.

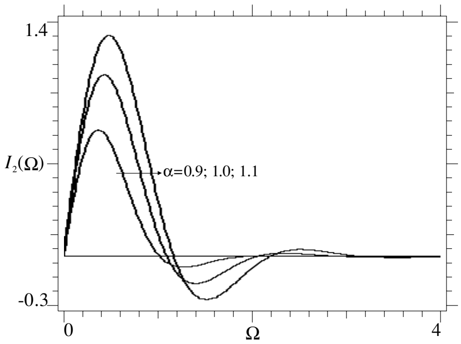

Figure 4. The function $I_2(\Omega)$ for $\alpha = 0.9, 1.0, 1.1$; $\beta = 1$; and $\gamma = 0.14$.

The stable and unstable manifolds of x_s intersect when the Melnikov function vanishes for some t_0, i.e., when $h(\Omega t_0) = (\tilde{\mu}/\tilde{\eta})(I_1/I_2(\Omega))$. We must distinguish between two cases.

For the values of Ω for which $I_2(\Omega)$ is positive we have that the previous equation has solution if and only if

$$\tilde{\eta} > \tilde{\mu}\frac{I_1}{I_2(\Omega)}\frac{1}{M^+}, \qquad M^+ = \max_{m\in[0,2\pi]}\{h(m)\} > 0, \quad (9)$$

while in the other case the solution exists if and only if

$$\tilde{\eta} > \tilde{\mu}\frac{I_1}{-I_2(\Omega)}\frac{1}{M^-}, \qquad M^- = -\min_{m\in[0,2\pi]}\{h(m)\} > 0. \qquad (10)$$

If we define

$$M(\Omega) = \begin{cases} M^+ & \text{if } I_2(\Omega) > 0, \\ M^- & \text{if } I_2(\Omega) < 0, \end{cases} \qquad (11)$$

we then have that homoclinic bifurcation occurs for

$$\tilde{\eta}_{\mathrm{cr}}(\Omega) = \tilde{\mu}\frac{I_1}{|I_2(\Omega)|}\frac{1}{M(\Omega)} = \tilde{\eta}_{\mathrm{cr}}^h(\Omega)\frac{1}{M(\Omega)}. \qquad (12)$$

When $N = 1$, we have $h(m) = \cos(m+\Psi_1)$ so that $M(\Omega) = 1$, and thus $\tilde{\eta}_{\mathrm{cr}}^h(\Omega)$ has the meaning of critical threshold for homoclinic bifurcation in the reference case of harmonic excitation. This curve is depicted in figure 5. Below $\tilde{\eta}_{\mathrm{cr}}^h(\Omega)$ there is no dynamic pull-in, while above it the erosion of the safe basin proceeds and dynamic pull-in becomes first impending (practically occurring only for *certain* initial conditions) and then, after complete erosion, inevitable, as it occurs for *all* initial conditions.

The most important characteristic of $\tilde{\eta}_{\mathrm{cr}}^h(\Omega)$, consequence of the zeros of $I_2(\Omega)$, is that it goes to infinity in correspondence with some 'anti-resonant' frequencies. This behaviour is not common for Melnikov analyses, but it has also been previously observed, for example, by Yagasaki [30, figure 3] in the analysis of the hardening Duffing equation with parametric and external harmonic excitations, and by the authors [29, figure 4] in the analysis of the single-well potential with two asymmetric escape directions (Helmholtz–Duffing equation) under external excitation.

For the case of figure 5 the first four anti-resonances are $\Omega_1 = 1.0998$, $\Omega_2 = 2.0421$, $\Omega_3 = 2.9918$ and $\Omega_4 = 3.9387$. If we proceed further, we note that $(\Omega_{i+2}-\Omega_{i+1})/(\Omega_{i+1}-\Omega_i) = 1$, $i \geqslant 1$, and this (i) suggests that there is an underlying

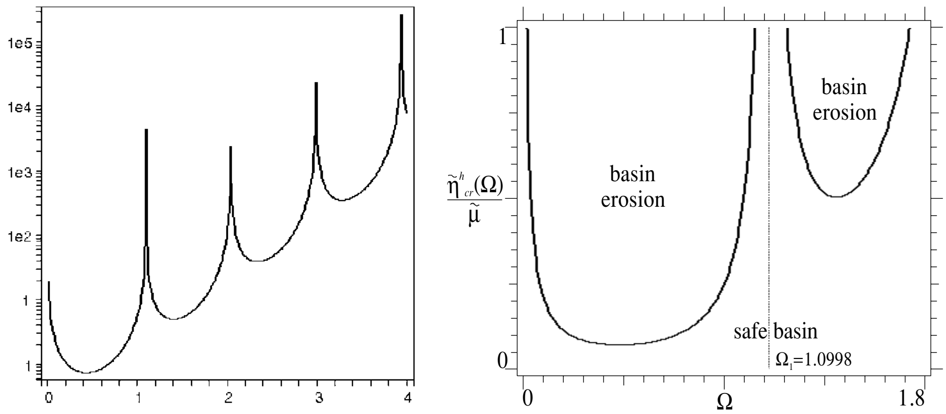

(*a*) (*b*)

Figure 5. The function $\tilde{\eta}^h_{\mathrm{cr}}(\Omega)/\tilde{\mu}$ for $\alpha = \beta = 1$ and $\gamma = 0.14$. (*a*) Large semi-logarithmic plot; (*b*) zoom for small and medium frequencies.

structure in the zeros of $I_2(\Omega)$ and (ii) permits computation of further critical frequencies.

Remark 2. From a physical point of view, it seems quite strange, at a first glance, that for a certain frequency the manifolds do not intersect even for extremely large excitation amplitudes. It can be conjectured that this is due to the first-order nature of the accomplished Melnikov analysis, and that higher order terms should be taken into account around these critical Ωs.

When the excitation is no longer harmonic, $M(\Omega) \neq 1$ and the critical threshold varies. For suitable choices of the excitation shape we are able to reduce $M(\Omega)$, and the homoclinic bifurcation threshold increases accordingly, $\tilde{\eta}_{\mathrm{cr}} > \tilde{\eta}^h_{\mathrm{cr}}$. Thus, we benefit from the superharmonics added to the reference harmonic term. This point is theoretically investigated in section 4, while numerical confirmation will be given in section 5.

4. Optimal control of homoclinic bifurcation

In this section, a method previously developed in [23, 29] and aimed at eliminating the homoclinic bifurcation is employed to control the nonlinear dynamics and the pull-in of the microbeam.

The idea of the control method is to increase the threshold $\tilde{\eta}_{\mathrm{cr}}(\Omega)$ for homoclinic bifurcation by optimally modifying the shape of the excitation. To quantitatively measure the improvement obtainable with respect to the reference harmonic excitation, the gain is introduced, which is defined as the ratio between the critical amplitudes of unharmonic and harmonic excitations,

$$G = \frac{\tilde{\eta}_{\mathrm{cr}}(\Omega)}{\tilde{\eta}^h_{\mathrm{cr}}(\Omega)} = \frac{1}{M(\Omega)}, \tag{13}$$

and depends only on the shape and not on the amplitude of the excitation.

It is now clear that the optimal excitation is obtained by solving the following problem:

$$\text{Maximize } G \text{ by varying the Fourier coefficients } h_j \text{ and } \Psi_j,\quad j = 2, 3, \ldots, \text{of } h(m). \tag{14}$$

This mathematical problem of optimization is exactly the same encountered in the application of the control method to other mechanical systems, and we refer, for example, to [23; section 3] for a detailed discussion and for the solutions under various assumptions. Here we consider only the case of a finite number of added superharmonics, which is most useful for applications.

When the excitation frequency Ω is such that $I_2(\Omega) < 0$, we have $M(\Omega) = -\min_{m\in[0,2\pi]} h(m)$ and the problem (14) reduces to

$$\text{Maximize } \min_{m\in[0,2\pi]} \{h(m)\} \text{ by varying } h_j \text{ and } \Psi_j,\ j = 2, 3, \ldots. \tag{15}$$

The solution of this problem for increasing number N of controlling superharmonics is given by $\Psi_j = 0$ and by the coefficients h_j reported in table 1 [23]. Note that, as expected, the optimal gain is an increasing function of N. For $N \to \infty$ it tends to 2, i.e., the homoclinic bifurcation threshold doubles, while quite good theoretical results can be obtained with even few added superharmonics.

Once the h_j are known from table 1, the excitation is given by

$$\eta(t) = \tilde{\eta} \sum_{j=1}^{N} \left(\frac{h_j I_2(\Omega)}{I_2(j\Omega)} \right) \sin(j\Omega t). \tag{16}$$

When $I_2(\Omega) > 0$, on the other hand, we have $M(\Omega) = \max_{m\in[0,2\pi]} h(m)$ and the problem (14) becomes

$$\text{Minimize } \max_{m\in[0,2\pi]} \{h(m)\} \text{ by varying } h_j \text{ and } \Psi_j,\ j = 2, 3, \ldots. \tag{17}$$

This problem is only seemingly different from (15). In fact, from $\max_{m\in[0,2\pi]}\{h(m)\} = -\min_{m\in[0,2\pi]}\{-h(m)\}$ we conclude that they are equivalent [29]. The solution of (17) is simply the solution of (15) with the even coefficients of table 1 taken with the minus sign, and the optimal excitation is still given by (16).

Previous optimization problems are frequency independent, so that their solutions and the associated optimal gains (table 1) do not depend on Ω [29]. This means that we are able to obtain Ω independent relative increments of the homoclinic bifurcation threshold. Furthermore, table 1 shows that these gains are large even with a single added superharmonic (41%) and reach a maximum of 100% with

Table 1. The numerical results of various optimization problems with an increasing finite number of superharmonics.

N	G_N	M_N	h_2	h_3	h_4	h_5	h_6	h_7	h_8	...
2	1.4142	0.7071	0.353 553							
3	1.6180	0.6180	0.552 756	0.170 789						
4	1.7321	0.5773	0.673 525	0.333 274	0.096 175					
5	1.8019	0.5550	0.751 654	0.462 136	0.215 156	0.059 632				
6	1.8476	0.5412	0.807 624	0.567 084	0.334 898	0.153 043	0.042 422			
7	1.8794	0.5321	0.842 528	0.635 867	0.422 667	0.237 873	0.103 775	0.027 323		
8	1.9000	0.5263	0.872 790	0.706 011	0.527 198	0.355 109	0.205 035	0.091 669	0.024 474	
...	...	...	...	...	...	...	...	...	...	...
∞	2	0.5	1	1	1	1	1	1	1	1

infinite superharmonics. In the region between $\tilde{\eta}_{\rm cr}$ and $\tilde{\eta}^h_{\rm cr}$ the control is theoretically effective: it is called 'saved region' and is depicted in figure 6 around $\Omega \cong 0.43$, corresponding to the first minimum of $\tilde{\eta}^h_{\rm cr}$.

Contrary to the optimal gain, the optimal excitation (16) is no longer Ω independent, and thus the actual cost of control (measured by the relative magnitude of the added superharmonics) varies with Ω. A critical case occurs, too. In fact, if the excitation frequency is such that $j\Omega$, $j = 2, 3, \ldots, N$, equals (or is very close to) one of the zeros of $I_2(\Omega)$, corresponding to the anti-resonance frequencies, the amplitude of the jth superharmonic tends to infinity (or becomes very large), and the excitation has no more physical meaning. In such a case, a different optimal solution of the problem (14) without the jth superharmonic must be looked for. This issue, however, is out of the scope of the present work, where it is assumed that $j\Omega$, $j = 2, 3, \ldots, N$, is far apart from the zeros of $I_2(\Omega)$. Note, however, that if Ω is close to one of those zeros, there is no control needed because no homoclinic bifurcation is actually predicted by the first-order Melnikov theory (see remark 2).

As an example, we have that for $\Omega = 0.7$ the optimal excitation for $N = 2$ is

$$\eta(t) = \tilde{\eta}[\sin(\Omega t) + 1.6591 \sin(2\Omega t)]. \tag{18}$$

It will be considered in the numerical simulations of the following section.

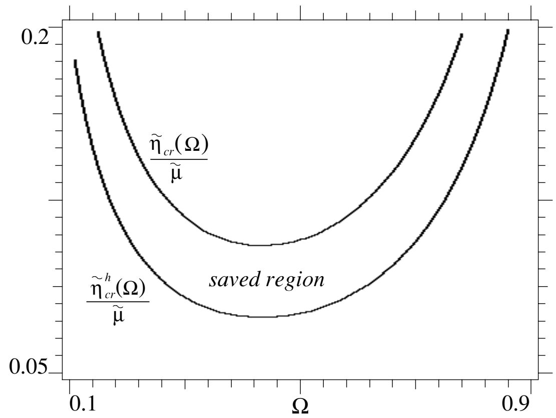

Figure 6. The homoclinic bifurcation threshold for harmonic ($\tilde{\eta}^h_{\rm cr}$) and optimal control ($\tilde{\eta}_{\rm cr}$) excitations and the saved region for the theoretical gain $G = 1.4142 (N = 2)$ and for $\alpha = \beta = 1$ and $\gamma = 0.14$.

5. Numerical simulations

Some numerical simulations aimed at highlighting system nonlinear dynamics and checking the practical performances of control are made. Following other studies [23, 24] which suggest that erosion is more marked close to resonance, we focus on the neighbourhood of $\Omega_{\rm res} = 0.7457$ which is the resonance frequency of $x_c = 0.219\,03$. In this range, we are not very far from the chaotic resonance $\Omega \cong 0.43$, and the bifurcation threshold occurs for an excitation amplitude still small (see figure 6; for example, $\tilde{\eta}^h_{\rm cr}(0.43) = \tilde{\eta}^h_{\rm cr\,min} = 0.074\,85\tilde{\mu}$ while $\tilde{\eta}^h_{\rm cr}(0.7) = 0.107\,84\tilde{\mu}$), so that its increment by means of control is highly welcome. In all forthcoming simulations, we will assume $\alpha = \beta = 1$, $\gamma = 0.14$ and $\tilde{\mu} = 0.01$.

5.1. Resonant behaviour with harmonic excitation

The resonant behaviour of (6) with harmonic excitation has the typical features of softening oscillators. To illustrate this fact, two relevant bifurcation diagrams, one for varying frequency and the other for varying amplitude, are reported in figures 7(*a*) and (*b*), respectively. The former shows the typical bending of the resonance curve towards lower frequencies, characteristic of softening oscillators. The latter shows the classical S-shape of the amplitude-response curves, and highlights the occurrence of the solely non-resonant oscillation for very small amplitudes, which is then flanked by the resonant oscillation originated from a (lower) SN bifurcation. The two attractors coexist up to disappearance of the non-resonant oscillation through an (upper) SN bifurcation. The resonant attractor survives up to the onset of a period doubling cascade eventually leading to escape from the potential well, i.e., to dynamic pull-in.

Several bifurcation diagrams like those of figure 7 have been made, and the overall scenario is summarized in the behaviour chart of figure 8, where the boundary crisis threshold at the end of the PD cascade and the homoclinic bifurcation threshold are reported, too. Figure 8 shares the same qualitative features of the behaviour chart of other softening oscillators, like, e.g., the Helmholtz oscillator [23, 31]. In particular, the V-shaped region of escape (which herein has the meaning of ultimate dynamic pull-in), whose vertex is at about $\Omega = 0.655$, is clearly recognizable, as well as the (lower right) degenerate cusp bifurcation at $\Omega = 0.737$ and $\tilde{\eta} = 0.000\,461$ where the two SN thresholds collapse.

5.2. Safe basin erosion with harmonic excitation

The erosion of the safe basins, which entails dynamic pull-in becoming more and more likely, is now discussed [25]

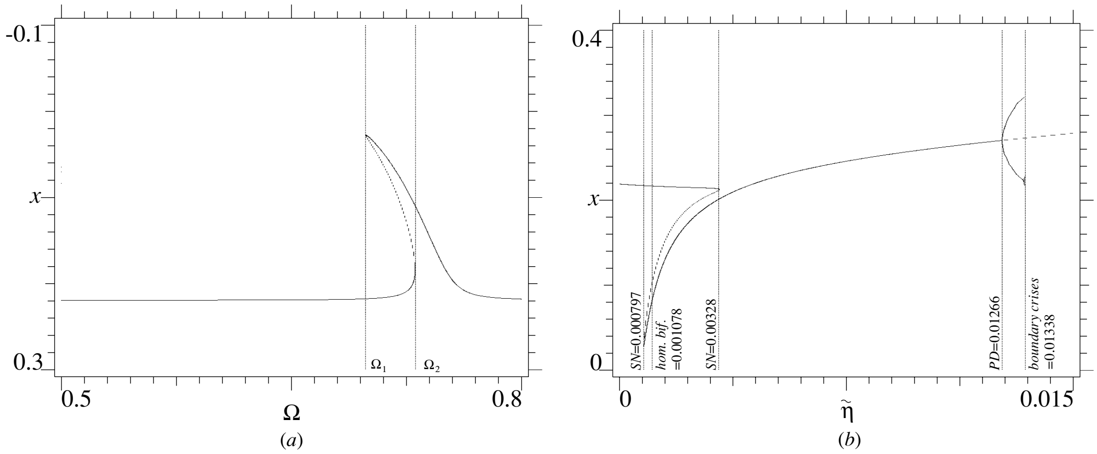

Figure 7. Bifurcation diagrams for (*a*) $\tilde{\eta} = 0.0008$, and (*b*) $\Omega = 0.7$, with harmonic excitation.

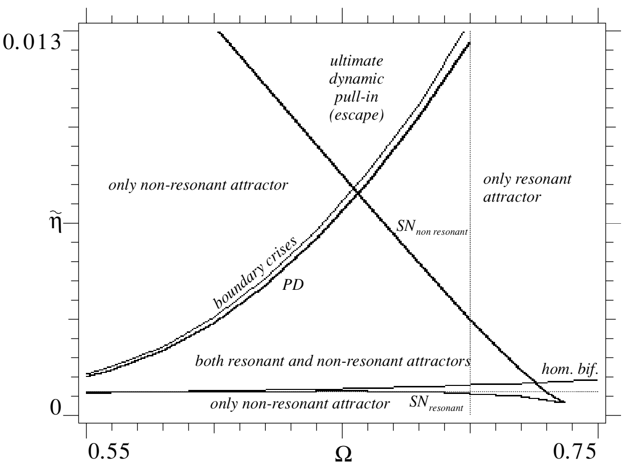

Figure 8. Frequency–amplitude behaviour chart of the system with harmonic excitation close to the resonance $\Omega_{\mathrm{res}} = 0.7457$. The dotted lines correspond to the bifurcation diagrams of figure 7.

by considering the value $\Omega = 0.7$ as representative of the resonant behaviour illustrated in the previous subsection. In this section, harmonic excitation is used to elaborate on the phenomenon, and is to be used later to estimate, by comparison, the effectiveness of control. In this case, the critical amplitude for homoclinic bifurcation is $\tilde{\eta}^h_{\mathrm{cr}} = 0.001\,078$ (figure 7(*b*)). We assume the microbeam to vibrate in a stationary regime, so that safe basins are just classical basins of attraction. Indeed, they are the union of the basins of all in-well bounded attractors (figure 9).

The erosion of the safe basins for increasing excitation amplitude is depicted in figure 9. The basin boundaries in the first two pictures are regular according to the excitation amplitude being less than $\tilde{\eta}^h_{\mathrm{cr}}$. In the first one (the static case) the unique attractor is x_c, while in the second one the resonant oscillations (dark grey) appear (see figure 7(*b*)). The amplitude value of the third picture is just above the homoclinic bifurcation, and accordingly the (white/greys) basin boundary has a very low degree of fractality. When the amplitude further increases, the classical mechanism [24] of incursion of fractal (white) tongues of the out-of-well attractor into the well is observed. Initially, it proceeds slowly, but a sudden incursion is noted at about $\tilde{\eta} = 0.0025$, likely due to the heteroclinic connection between the hilltop saddle x_s and the saddle x'_s

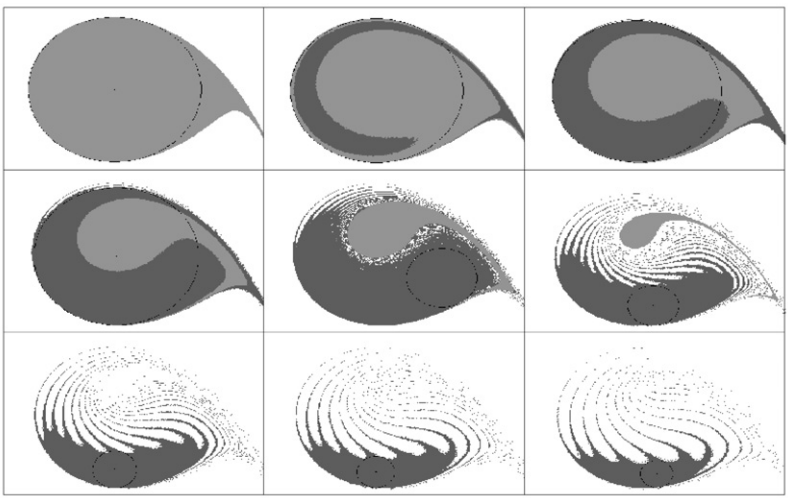

Figure 9. Safe basins for $\Omega = 0.7$ and for $\tilde{\eta} = 0.0000$ (upper left), 0.0010, 0.0015, 0.0020, 0.0025, 0.0030, 0.0035, 0.0040, 0.0045 (bottom right). For each picture $-0.1 < x < 0.65$ and $-0.22 < y < 0.22$. The safe basin is the union of all grey basins of attraction. The circles are those used in the definition of the integrity factor.

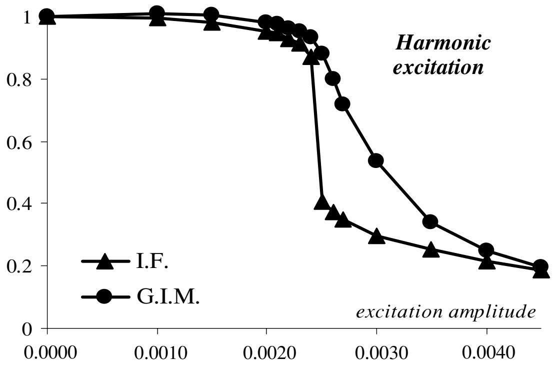

Figure 10. Erosion profiles for two different integrity measures, $\Omega = 0.7$.

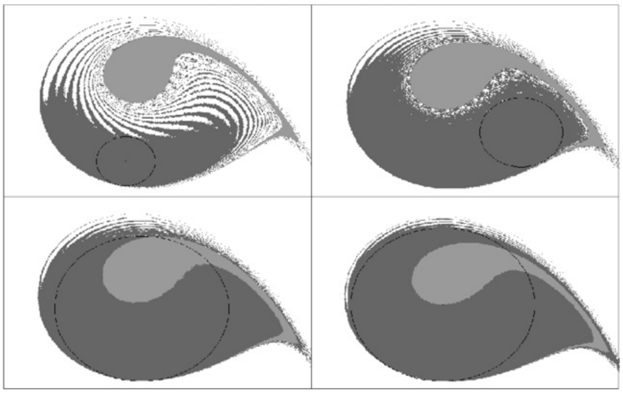

Figure 11. Safe basins for $\Omega = 0.7$, $\tilde{\eta} = 0.0025$ and for (*a*) $\eta_2/\eta_1 = -1.5$ (upper left), (*b*) $\eta_2/\eta_1 = 0$ (harmonic), (*c*) $\eta_2/\eta_1 = 0.5$ and (*d*) $\eta_2/\eta_1 = 1.6591$ (optimal, bottom right). For each picture $-0.1 < x < 0.65$ and $-0.22 < y < 0.22$.

on the inner boundary separating the basins of resonant and non-resonant attractors. After this event, the erosion rapidly develops, and pull-in becomes very likely, although there still survive initial conditions not leading to pull-in.

It is worth noting that only the resonant attractor basin is eroded, while the non-resonant one (light grey) remains uneroded, as being protected by the stable manifolds of x_s', up to finally disappearing through SN bifurcation (see figure 7(*b*)). This behaviour is certainly welcome from a practical point of view. However, it also has a drawback, because when the non-resonant solution disappears, its residual basin being surrounded by the white one, the system certainly undergoes dynamic pull-in. This may be very dangerous in applications, where for a safe use one must be sure that the response has previously switched to the surviving resonant solution.

The final part of the basin erosion phenomenon proceeds fairly slowly up to complete vanishing of in-well solutions. The final escape corresponding to ultimate pull-in occurs for a very large excitation amplitude ($\tilde{\eta} = 0.013\,38$, see figure 7(*b*)) and is not shown in figure 9, where the largest considered amplitude already corresponds to a residual and practically useless safe basin.

A measure of the integrity of the safe basin must be chosen to quantify the erosion shown in figure 9. This is a very important issue which is herein addressed by considering two different measures [25]: the global integrity measure (GIM), representing the (normalized) area of the safe basin, and the integrity factor (IF), representing the (normalized) radius of the largest circle entirely contained in the safe basin, as shown in figure 9. The former is a natural and easy measure, but it does not properly take into account the fractal tongues eroding the safe basin, which are instead better considered by the IF. In fact, the latter is a measure of the 'compact' core of the safe basin, to be reliably referred to in practical applications.

By plotting the integrity measure as a function of the increasing excitation amplitude we obtain the erosion profiles of figure 10. Both start to significantly decrease at about $\tilde{\eta} = 0.0025$, highlighting the likely occurrence of the secondary event quoted before. But only the IF profile sharply falls down due to the instantaneous penetration of white tongues from outside (see figure 9), with the ensuing safety reduction, which is correctly accounted for by this measure. Figure 10 further shows that in any case, i.e., even far from the fall, the IF is more conservative and thus more reliable for practical applications.

5.3. Reduction of erosion by control

In this section, the effectiveness of control in shifting erosion towards higher amplitudes is investigated. First, it is worth pointing out what can be theoretically expected, and what cannot. In fact, by noting that the erosion is triggered by the homoclinic bifurcation and that this is shifted by control, we can certainly expect some improvements. What cannot be predicted, on the other hand, is the actual extent of this benefit. Indeed, the homoclinic bifurcation is not directly involved in the successive topological events (e.g., the guessed secondary heteroclinic bifurcation) underlying the erosion, though being somehow a relevant basic prerequisite. Thus, the aim of this section is to quantify the practical performances of control, possibly above the theoretical predictions.

We consider control with a single added superharmonic, i.e., we consider the excitation (18) and the saved region of figure 6. More refined control excitations will certainly provide better results.

We start by studying the effects of the added superharmonic for fixed parameters. For $\Omega = 0.7$, $\tilde{\eta} = 0.0025$, we report in figure 11 the basins of attraction for various superharmonic relative amplitudes η_2/η_1. The case of harmonic excitation with the associated eroded basin boundary is also reported for comparison in figure 11(*b*). The addition of the superharmonic term is indeed able to significantly reduce the erosion, as clearly shown in figure 11(*c*). Then, by increasing η_2/η_1 up to the optimal value 1.6591 (figure 11(*d*)), the erosion is further reduced. The crucial role of the added superharmonic is underlined by figure 11(*a*), which shows the dramatic effects obtained if the superharmonic is not properly chosen, in particular if considering a wrong sign corresponding to a half period phase shift.

The good practical performance of control clearly visible in figure 11 is confirmed and summarized by the profiles of figure 12(*a*) reporting the normalized IF and GIM, divided by the value of the harmonic excitation measure, as functions of the superharmonic relative amplitude η_2/η_1. Thus, the curves of figure 12(*a*) are indeed *practical* gains.

The resemblance of the numerical profiles with the *theoretical* curve $G = G(h_2)$, reported in figure 12(*b*), is noticeable, from both a qualitative and a quantitative point

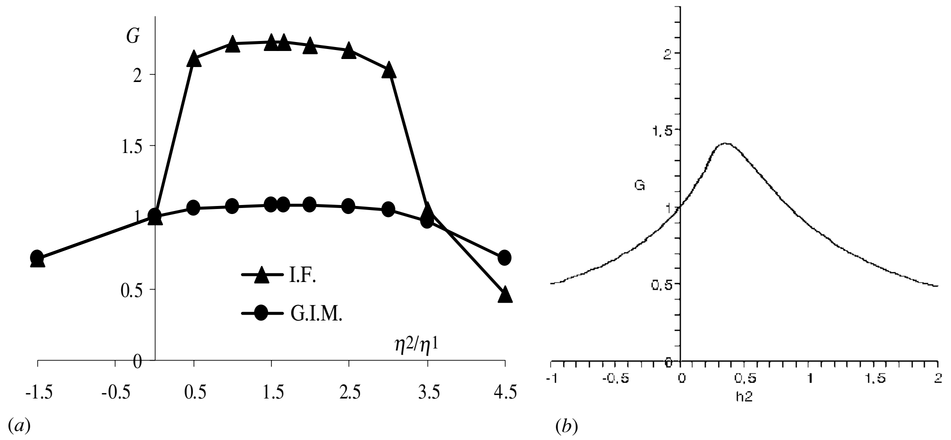

Figure 12. (*a*) The numerical gains, i.e., the IF and GIM normalized to 1 in correspondence to the harmonic excitation, as a function of the superharmonic relative amplitude η_2/η_1. $\Omega = 0.7$ and $\tilde{\eta} = 0.0025$. (*b*) The theoretical gain G as a function of the superharmonic coefficient h_2.

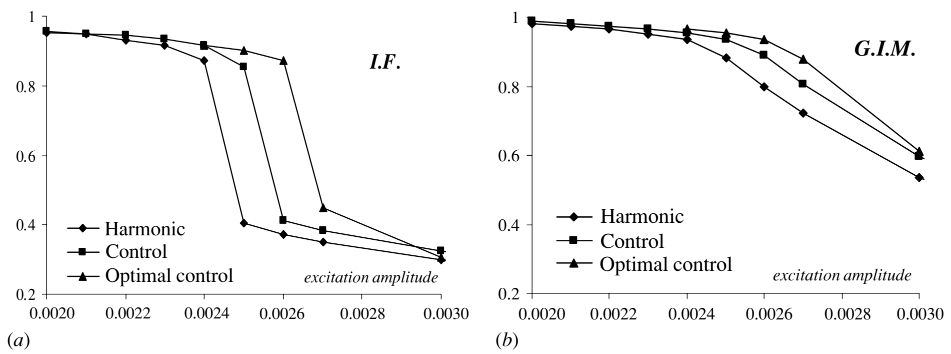

Figure 13. Erosion profiles for harmonic ($\eta_2/\eta_1 = 0$), control ($\eta_2/\eta_1 = 0.5$) and optimal control ($\eta_2/\eta_1 = 1.6591$) excitations for $\Omega = 0.7$.

of view. In fact, the maximum of all curves is attained for the same value of the independent variables (remember that, by (8), $h_2 = (\eta_2/\eta_1)(I_2(2\Omega)/I_2(\Omega)) = 0.213\eta_2/\eta_1$), proving that the theoretical optimal superharmonic provides optimal practical results. We can then conclude that theoretical predictions are well verified in practice, somehow beyond expectations, because the controlled homoclinic bifurcation only triggers the erosion and is not directly involved in the subsequent basin evolution, so that some major discrepancies would not actually be surprising.

While sharing these overall features, the three curves of figure 12 have some specific differences basically due to the fact that the instantaneous penetration of fractal tongues has a dramatic effect on safe basins (see figures 9 and 11). This phenomenon is well described by the IF and poorly described by the GIM, as already stated, and is responsible for sharpness of the IF profile versus dullness of the GIM profile (as in figure 10), and for the difference between theoretical and practical optimal gains, which stands as the major result. In particular, with the IF, the optimal gain is about 2.22, which is significantly larger than the theoretical value 1.41, thus showing how practical performances are somehow better than theoretical expectations; instead, with the GIM, the optimal gain is significantly smaller, being about 1.08. Yet, it is still larger than 1, thus showing how this measure is also capable of highlighting the benefits of control, though to a reduced extent. These results suggest that, again, the IF is a better measure of integrity in practical applications.

An important conclusion which can be drawn from figures 11 and 12 is that quite good results can be obtained with a superharmonic even smaller than the optimal one, at least for that specific case. This is due to the fact that, e.g., for $\eta_2/\eta_1 = 0.5$ the theoretical and practical gains are still larger than 1, though not being optimal. This may be useful in applications, because the optimal excitation, which involves a superharmonic larger than the basic harmonic, may be too much expensive, and one may prefer cheaper excitations providing still satisfactory, although not optimal, results.

The erosion profiles obtained around the critical amplitude $\tilde{\eta} = 0.0025$ (see figure 10) with harmonic ($\eta_2/\eta_1 = 0$), control ($\eta_2/\eta_1 = 0.5$), and optimal control ($\eta_2/\eta_1 = 1.6591$) excitations are compared in figure 13. The first point highlighted by the overall shift of the profiles is that the previous observations on control effectiveness, made for a fixed amplitude value, do extend and generalize.

Figure 13 shows that, according to theoretical predictions, when η_2 increases, the profile is initially moved towards higher excitation amplitudes. The forward shift continues up to the optimal value $\eta_2/\eta_1 = 1.6591$, above which further increasing η_2 would entail backward shift of the profile towards that of the harmonic excitation (see figure 12).

Both the considered measures are able to highlight the improvement of control. In particular, the horizontal shifts of the profiles are comparable, while the vertical shift for a fixed amplitude is more marked with the IF, due to the sharpness of its profile, thus showing once again to be a better integrity measure.

Figure 13(*a*) shows that there is a well-defined interval of amplitudes where the erosion reduction achieved through control is very large, the safe basin being almost maintained with optimal control and more than halved with harmonic excitation. In particular, the saved interval is approximately $0.0025 < \tilde{\eta} < 0.0027$ with optimal control, while reducing to $0.0025 < \tilde{\eta} < 0.0026$ with non-optimal control. This agrees with the theoretical predictions which suggest that the latter still provides good results (the gain being larger than 1), although worst than those given by the optimal excitation.

What the control is not able to do is change the pattern of the erosion profiles. For example, those of figure 13(*a*) remain as sharp as the original one, and do not become dull, which would be desirable from a practical viewpoint because it would entail a non-instantaneous fall towards unsafe regimes. However, they do not become sharper, which would be very dangerous. This conclusion, however, is strictly related to the considered value of the excitation frequency, and cannot be generalized. In fact, for the Helmholtz oscillator, which has similar features for being mechanically comparable, the erosion becomes sharper for frequencies below the vertex of the V-shaped region of escape (see figures 13(*a*) and (*b*) of [23]), and this phenomenon is likely to occur also for the present oscillator.

6. Conclusion

A control method aimed at shifting towards high excitation amplitudes the homoclinic bifurcation of a nonlinear thermoelastic electrodynamically actuated microbeam has been applied. The practical goal of the method is that of shifthing towards higher excitation amplitudes the dynamic pull-in representing the failure phenomenon of several MEMS devices.

The optimization problem for determining the optimal controlling superharmonics to be added to a basic harmonic excitation has been stated and solved, by taking advantage from the fact that it is the same encountered in the application of the control method to different mechanical systems. As a matter of fact, this further confirms the generality of the control method investigated in [29].

Extensive numerical simulations have been performed with the aim of studying the system nonlinear dynamics and checking the practical performances of control.

First, the system response with harmonic excitation in the neighbourhood of classical resonance has been illustrated by means of bifurcation diagrams and a behaviour chart looking like the corresponding one of analogous (e.g., Helmholtz) mechanical oscillators.

Then, attention has been focused on the safe basin erosion governing the system dynamical integrity, and being thus related to its practical use. In fact, reduction of dynamical integrity up to final dynamic pull-in entails a definite loss of system reliability.

Two integrity measures, GIM and IF, have been considered and compared with each other making reference to the erosion profiles for increasing excitation amplitudes, and it has been shown that the former fails in highlighting the instantaneous penetration of fractal tongues from outside.

Then, the overall ability of control in shifting the erosion profiles towards higher excitation amplitudes has been highlighted. This represents the major practical benefit, and a very important and somehow unexpected result, which extends the control effectiveness well beyond the limits corresponding to theoretical gain. It is also worth mentioning that, in this work, only one controlling superharmonic has been employed, and better results can certainly be obtained if using more superharmonics.

Other system configurations (boundary conditions, position of the electric force, etc), MEMS devices, and/or numerical values of the parameters can easily be considered. However, this is in order mostly to highlight possibly different features of system response, and is thus left for future works.

A less trivial modification would occur in the case of two symmetrically placed substrates. In this case, the unique potential well is laterally bounded by two symmetrically placed saddles, and is surrounded by two heteroclinic orbits instead of a single homoclinic one. The control method can be applied following the lines illustrated in [29] for the case of the softening Duffing oscillator, which is qualitatively similar to the two-substrate system.

References

[1] Gottlieb O and Champneys A R 2005 Global bifurcations of nonlinear thermoelastic microbeams subject to electrodynamic actuation IUTAM Symp. on Chaotic Dynamics and Control of Systems and Processes in Mechanics *Solid Mechanics and Its Applications* vol 122 ed G Rega and F Vestroni (Berlin: Springer) pp 47–57

[2] Pelesko J A and Bernstein D H 2002 *Modeling MEMS and NEMS* (London/Boca Raton, FL: Chapman and Hall/CRC Press)

[3] Burdess J S 1999 Modelling of nonlinearities in MEMS devices *IEE Seminar on Microengineering, Modelling and Design* p 42

[4] Adams S G, Bertsch F and MacDonald N C 1996 Independent yuning of the linear and nonlinear stiffness coefficients of a micromechanical device *MEMS'96: Proc. 9th IEEE Int. Workshop on Micro Structures, Sensors, Actuators, Machines and Systems* pp 32–7

[5] Lifshiz R and Roukes M L 2000 Thermoelastic damping in micro- and nanomechanical systems *Phys. Rev.* B **61** 5600–9

[6] Zhao X, Dankowicz H, Reddy C K and Nayfeh A H 2004 Modelling and simulation methodology for impact microactuators *J. Micromech. Microeng.* **14** 775–84

[7] Cao D Q, Liu D and Wang C H-T 2005 Nonlinear dynamic modelling for MEMS components via the cosserat rod element approach *J. Micromech. Microeng.* **15** 1334–43

[8] Wang C, Liu D, Rosing R, De Masi B and Richardson A 2004 Construction of nonlinear dynamic MEMS component models using cosserat theory *Analog Integr. Circuits Signal Process.* **40** 117–30

[9] Wolf K and Gottlieb O 2002 Nonlinear dynamics of a noncontacting atomic force microscope cantilever actuated by a piezoelectric layer *J. Appl. Phys.* **91** 4701–9

[10] Adbel-Rahman E M, Younis M I and Nayfeh A H 2003 A nonlinear reduced-order model for electrostatic MEMS *Proc. ASME 2003 Design Eng. Tech. Conf. (Chicago, USA, 2–6 Sept.)* (paper DETC2003/Vib-48517)

[11] Hung E S and Senturia S D 1999 Generating efficient dynamical models for microelectromechanical systems

from a few finite-element simulation runs *IEEE J. Microelectron. Syst.* **8** 280–9
[12] Krylov S, Harari I and Cohen Y 2005 Stabilization of electrostatically actuated microstructures using parametric excitation *J. Micromech. Microeng.* **15** 1188–204
[13] Zhao X, Abdel-Rahman E M and Nayfeh A H 2004 A reduced-order model for electrically actuated microplates *J. Micromech. Microeng.* **14** 900–6
[14] Nayfeh A H, Younis M I and Abdel-Rahman E 2005 Reduced-order models for MEMS applications *Nonlinear Dyn.* **41** 211–36
[15] Davis W O, O'Reilly O M and Pisano A P 2004 On the nonlinear dynamics of tether suspensions for MEMS *ASME J. Vib. Acoust.* **126** 326–31
[16] Liu S, Davidson A and Lin Q 2004 Simulation studies on nonlinear dynamics and chaos in a MEMS cantilever control system *J. Micromech. Microeng.* **14** 1064–73
[17] Wang Y C, Adams S G, Thorp J S, MacDonald N C, Hartwell P G and Bertsch F 1998 Chaos in MEMS, parameter estimation and its potential application *IEEE Trans. Circuits Syst.* I **45** 1013–20
[18] Ashhab M, Salapaka M V, Dahleh M and Mezic I 1999 Melnikov-based dynamical analysis of microcantilevers in scanning probe microscopy *Nonlinear Dyn.* **20** 197–220
[19] Ashhab M, Salapaka M V, Dahleh M and Mezic I 1999 Dynamical analysis and control of microcantilevers *Automatica* **35** 1663–70
[20] Sulfridge M, Saif T, Miller N and Meinhart M 2004 Nonlinear dynamics study of a bistable MEMS: model and experiment *IEEE J. Microelectron. Syst.* **13** 725–31
[21] Krylov S and Maimon R 2003 Pull-in dynamics of an elastic beam actuated by distributed electrostatic force *Proc. of ASME 2003 Design Eng. Tech. Conf. (Chicago, USA, 2–6 Sept.)* (paper DETC2003/Vib-48518)
[22] Nayfeh A H, Younis M I and Abdel-Rahman M 2005 Dynamic pull-in phenomenon *MEMS resonators* submitted
[23] Lenci S and Rega G 2003 Optimal control of homoclinic bifurcation: theoretical treatment and practical reduction of safe basin erosion in the Helmholtz oscillator *J. Vib. Control* **9** 281–316
[24] Thompson J M T 1989 Chaotic behavior triggering the escape from a potential well *Proc. R. Soc.* A **421** 195–225
[25] Rega G and Lenci S 2005 Identifying, evaluating, and controlling dynamical integrity measures in nonlinear mechanical oscillators *Nonlinear Anal.* **63** 902–14
[26] Wiggins S 1988 *Global Bifurcation and Chaos: Analytical Methods* (New York: Springer)
[27] Chen G and Dong X 1998 *From Chaos to Order: Methodologies, Perspectives and Applications* (Singapore: World Scientific)
[28] Ashhab M, Salapaka M V, Dahleh M and Mezic I 1997 Control of chaos in atomic force microscopes *Proc. American Control Conference (Albuquerque, New Mexico, June)* pp 192–202
[29] Lenci S and Rega G 2004 A unified control framework of the nonregular dynamics of mechanical oscillators *J. Sound Vib.* **278** 1051–80
[30] Yagasaki K 1991 Chaos in a weakly nonlinear oscillator with parametric and external resonances *ASME J. Appl. Mech.* **58** 244–50
[31] Szemplinska-Stupnicka W 1992 Cross-well chaos and escape phenomena in driven oscillators *Nonlinear Dyn.* **3** 225–43